Journal of Materials Chemistry A

Accepted Manuscript

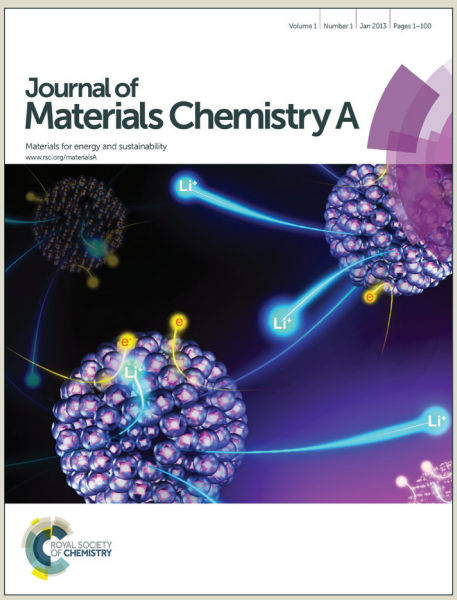

ROYAL SOCIETY OF CHEMISTRY

www.rsc.org/materialsA

Ti-substituted $Li[Li_{0.26}Mn_{0.6-x}Ti_xNi_{0.07}Co_{0.07}]O_2$ layered cathode material with improved structural stability and suppressed voltage fading

Zhaoxin Yu,[a] Shun-Li Shang,[b] Mikhail. L. Gordin,[a] Adnan Mousharraf,[a] Zi-Kui Liu,*[,b] and Donghai Wang*[,a]

[a]Department of Nuclear and Mechanical Engineering, The Pennsylvania State University, University Park, Pennsylvania 16802, United States

[b]Department of Materials Science and Engineering, The Pennsylvania State University, University Park, Pennsylvania 16802, United States

Note: *Supporting Information* (SI) included.

ABSTRACT: Despite considerable effort, practical application of high-energy-density, lithium (Li)- and manganese (Mn)-rich layered cathode materials remains difficult due to the low first cycle efficiency, poor structural stability, and the consequent voltage fading. In the present work, the Li- and Mn-rich layered cathodes of $Li[Li_{0.26}Mn_{0.6-x}Ti_xNi_{0.07}Co_{0.07}]O_2$ ($0<x<0.1$) with various titanium (Ti) compositions were synthesized and their electrochemical properties were evaluated. It was found that Ti substitution greatly improves the structural stability of the Li- and Mn-rich layered cathode materials, extending the cathode's cycle life and mitigating the voltage fading. The present first-principles analyses of the cohesive energy, phonon force constants, and charge density of these materials indicate that Ti substitution increases the stability of the layered structure and prevents Mn ions migration from transitional metal layer to adjacent Li-ion layer. These theoretical analyses coincide with the present experimental results and provide the underlying mechanism behind the improved cycling stability and weakened voltage fading.

Key words: Lithium-rich and manganese-rich; cathode; voltage fading; first-principles and phonon calculations

■INTRODUCTION

The rapid proliferation of portable electronics and the growth of emerging technologies like electric vehicles and intermittent renewable energy generation have led to huge demand for energy storage, and thereby to unprecedented efforts to develop high performance rechargeable batteries.[1-8] Lithium-ion (Li-ion) batteries have become especially popular due to their relatively good energy and power densities, but are now having difficulty meeting the needs of the cutting-edge applications. The materials used in Li-ion batteries, especially the cathode materials, play a dominant role in determining battery performance.[9-14] Layered structured cathode has been well studied. $LiCoO_2$ as a mature commercial cathode material in the past decades is a good example. Cycling between 3 to 4.2 V, $LiCoO_2$ delivers a practical specific capacity of 130 – 140 $mAhg^{-1}$ and shows a good cycling stability. However, compared to its theoretical capacity of 272 $mAhg^{-1}$, only one half of Li extracts from the structure. Charging to higher voltage could increase the capacity, which, unfortunately, would destroy structural and chemical stability of electrode, leading to fast capacity decay.[15] After commercial use of $LiCoO_2$, layered $LiNi_{1/3}Mn_{1/3}Co_{1/3}O_2$ and $LiNi_{0.85}Co_{0.1}Al_{0.05}O_2$ attract the attention due to their higher capacity than that of $LiCoO_2$, but still less than 200 $mAhg^{-1}$.[16, 17] Recently, a new class of Li- and manganese (Mn)-rich layered cathode materials with a high capacity of over 220 $mAhg^{-1}$ has been discovered: Li_2MnO_3-stabilized $LiMO_2$ with M being the transition metals like Co, Mn, and Ni.[18-23] The formula of $xLi_2MnO_3 \cdot (1-x)LiMO_2$ or $Li[Li_\eta Mn_{1-y-z}Ni_yCo_z]O_2$ is widely used to represent this class of

materials.[6, 24] Although Li_2MnO_3 is inert for Li-ion insertion/extraction in the voltage range of 2.0 – 4.4 V, it can be activated by increasing charging voltage up to 4.8 V to electrochemically remove Li_2O from Li_2MnO_3.[25] After Li_2O removed from Li_2MnO_3 during the activation process, the remaining MnO_2 can host additional Li ions to form $LiMnO_2$, leading to a high specific capacity above 210 $mAhg^{-1}$.[26] Therefore, the high working voltage (up to 4.8 V) and the great specific capacity (above 220 $mAhg^{-1}$) make $Li[Li_\eta Mn_{1-y-z}Ni_yCo_z]O_2$ a promising cathode material. However, it is well known that high spin Mn^{3+}ions in $LiMnO_2$ may induce Jahn-Teller distortion.[27-30] Two Mn^{3+} ions change to one Mn^{2+} and one Mn^{4+}. Mn^{2+} can diffuse to octahedral sites in the adjacent Li-ion layer, forming a spinel-like structure with the rearrangement of Li, Mn, and O atoms.[31, 32] The structural instability results in both poor cycling performance and severe voltage fading.[33, 34] Up to date, this material is still far from practical applications due to these technical hurdles. Accordingly, extensive efforts have been made to improve the structure stability, expand cycling life, and mitigate voltage fading.[9-11]

Elemental substitution or atom doping is one of the effective methods to improve electrochemical performance of the Li- and Mn-rich layered cathode materials in Li-ion batteries. In particular, substitutions of (i) Na^+ for Li^+ in $Li_{2-x}Na_xMn_2O_3$ and $Na_xLi_{1.2-x}Mn_{0.54}Ni_{0.13}Co_{0.13}O_2$,[19, 35] and (ii) M^{3+}=Al^{3+}, Cr^{3+}, Fe^{3+}, Co^{3+}, and Ga^{3+} for Mn^{4+} and Ni^{2+} in $Li_{1.2}Mn_{0.6-0.5x}Ni_{0.2-0.5x}M_xO_2$ effectively improve the capacity retention and/or rate performance.[24, 36-38] Na^+ substitution helps to decrease the grain size and charge transfer resistance, and to increase the crystallinity and the Li-ion diffusion coefficient. M^{3+} substitution could increase the average oxidation state of the transitional metal (e.g. Mn cation from 3+ to 3.3+) and suppress the John-Teller effect, resulting in a better cycling performance.[29] Recently, substitution of Ti^{4+}

for Mn^{4+}in Li- and Mn-rich cathode material has been reported to be effective in suppressing oxygen release. It is due to the higher bonding energy of Ti-O than that of Mn-O, indicating that Ti substitution helps to increase the structure stability.[24, 36] Also, Li_2TiO_3 has been introduced into $LiNi_{0.5}Mn_{0.5}O_2$ composite, serving as structure stabilizer to improve the electrochemical performance.[39] Ti substitution has also been reported in the spinel cathode $LiMn_{2-x}Ti_xO_4$, which leads to higher cycling retention and better rate capability.[29] It's clear that Ti substitution could help to improve the electrochemical performance by stabilizing structure. However, it is still interesting to know if and how Ti substitution can affect the transition metal (e.g. Mn^{4+}) around it and help to suppress the voltage fading in the Li- and Mn-rich layered oxide cathode.

The present work aims to address the aforementioned questions by combining experimental studies and theoretical analyses. Ti-substituted Li- and Mn-rich layered cathode materials ($Li[Li_{0.26}Mn_{0.6-x}Ti_xNi_{0.07}Co_{0.07}]O_2$, $0<x<0.1$) were prepared and their electrochemical performances were characterized to determine the effects of Ti on improving cycling stability and mitigating voltage fading. The density functional theory (DFT) based first-principles and phonon calculations were carried out to investigate the energetics of Ti substitution on structure transformation from layer to spinel. We find that alloying element Ti substitution indeed extends the cathode's cycling life and weakens the voltage fading. DFT based phonon force constants show that the Mn-Ti pair is characterized as the strongest interaction within the metal-sublattice, indicating the role of Ti in stabilizing the Mn ion. Additionally, the range of charge loss for Ti is the largest one among all metals (such as Mn, Co, Ni…), implying that the addition of Ti stabilizes the layered structure, and in turn, extends the cycling life and weakens the voltage fading.

■ EXPERIMENTAL AND COMPUTATIONAL METHODS

Materials Preparation. Reference and Ti-substituted cathode materials, $Li[Li_{0.26}Mn_{0.6-x}Ti_xNi_{0.07}Co_{0.07}]O_2$ (x = 0, 0.037, and 0.074), were prepared from LiOH (Sigma-Aldrich, ≥98%), TiO_2 (Alfa Aesar, 99.9%), and Mn-Ni-Co hydroxide precursors. The transition metal hydroxide precursors were synthesized by co-precipitation as follows. 2.4 ml of 14M ammonia aqueous solution (Ward's Science, 28~30%, 14M), serving as a chelating agent, was added into 100ml of aqueous solution of $NiSO_4 \cdot 6H_2O$ (Alfa Aesar, 98%), $MnSO_4 \cdot H_2O$ (Sigma Aldrich, ≥99%), and $CoSO_4 \cdot 7H_2O$ (Sigma Aldrich, ≥99%) (with the concentration of total transitional metal $M^{2+}$of 0.12M) in a three-neck round flask. 25ml of 1M sodium hydroxide (NaOH) solution was then added to the flask by drop under argon atmosphere protection. The operation temperature (60ºC) and the stirring speed (1000 rpm) in the flask were carefully controlled. The as-prepared $Mn_{0.8-x}Ni_{0.1}Co_{0.1}(OH)_{2(1-x)}$ precursor was washed with distilled water for several times, and dried at 100 ºC for 5h. The precursor was mixed thoroughly with a stoichiometric amount of TiO_2 and 10% over the stoichiometric LiOH (the excess LiOH was used to compensate for possible Li loss during the following calcination[26, 38]). The mixture was then calcined at 900 ºC for 10h to obtain the $Li[Li_{0.26}Mn_{0.6-x}Ti_xNi_{0.07}Co_{0.07}]O_2$ powder.

First-Principles and Phonon Calculations. All DFT-based first-principles calculations in the present work were performed using the VASP 5.3 code,[40] together with the exchange-correction functional described by an improved generalized gradient approximation for densely packed solids and their surfaces (PBEsol).[41] Calculations were performed on the lowest energy structure with the same kind of metals as far (dispersion) as possible within the metal-sublattice, viz., the maximum entropy probability distribution (MEPD),[42] see Supporting Information (SI) for details.

In order to take into consideration the strong on-site Coulomb interaction (U) presented in the localized 3*d* electrons of the magnetic elements Mn, Co, and Ni,[43] the PBEsol+U calculations were performed. To further verify structural stability as well as quantitative interactions between each atomic pair in $Li_9(X_1Y_1Z_1Mn_6)O_{18}$ (see details below). Phonon calculations were performed using the YPHON code:[44] a parameter-free, mixed-space approach developed recently in our group. More details regarding first-principles and phonon calculations were given in the SI.

Characterization. Power X-ray diffraction (XRD) was performed on a Rigaku Miniflex II spectrometer with Cu K_α radiation. The morphology of $Li[Li_{0.26}Mn_{0.6-x}Ti_xNi_{0.07}Co_{0.07}]O_2$ was investigated with a FEI Nova NanoSEM 630 field emission scanning electron microscope (FE-SEM) and FEI Titan^3 G2 dual aberration corrected scanning/transmission electron microscope (S/TEM). X-ray photoelectron spectroscopy (XPS) measurement was carried out with a Kratos XSAM800 Ultra spectrometer. All data was calibrated against the C 1s peak at 285 eV.

Electrochemical Measurements. Electrode slurry was made by mixing the as-prepared materials, Super P carbon black, and polyvinylidene fluoride (PVDF) with a weight ratio of 7:2:1 inn-methyl-2-pyrrolidone (NMP) solution. The slurry was stirred overnight, coated onto aluminum foil, and dried at 100ºC overnight to prepare electrode sheets. Coin-cell-sized electrodes were then punched from this sheet. Coin cells (CR-2016) were assembled in an Ar-filled glove box (MBraun, Inc.), with 1M $LiPF_6$ solution in a mixed solvent of ethylene carbonate (EC) and diethyl carbonate (DEC) (1:1, v/v) as the electrolyte, lithium metal as the counter electrode (anode), and Celgard 2400 polypropylene membrane as the separator. Cells were

cycled galvanostatically in the voltage range of 2.0 – 4.8V at room temperature using a BTS-5V1 mA Neware battery test system.

■ RESULTS AND DISCUSSION

Figure 1a illustrates powder XRD patterns of the reference and Ti-substituted samples of $Li[Li_{0.26}Mn_{0.6-x}Ti_xNi_{0.07}Co_{0.07}]O_2$ (x = 0, 0.037 and 0.074), with silicon (Si) powder as internal standard. XRD peaks corresponding to Si (PDF #04-012-7888) are marked as yellow square. All of the strong peaks can be indexed to a rhombohedral phase with space group $R\bar{3}m$, which is normally taken as the signature of the $LiMO_2$ phase.[28, 42] Several weak peaks located in the range of 20 – 23º (2θ values, unless noted otherwise) are consistent with the $LiMn_6$ super-ordering in the Li_2MnO_3 monoclinic phase with C2/m symmetry. No impurity phases are detected for all three samples. The magnified region of 43 – 46º is also shown in Figure 1b to clearly display the peak shift with increasing Ti content. The peak of (104) plane located at ~44.7° for the Ti-free sample, shifts to larger d-spacing between the (104) planes with increasing Ti content. Given the larger radius of Ti^{4+} (0.605 Å) compared to that of Mn^{4+} (0.53 Å)[27], this indicates that Ti^{4+} was successfully integrated into the lattice and substituted for Mn^{4+}. To further confirm Ti substitution, XRD Rietveld refinements of all three samples were conducted as shown in Figure S1a – 1c, where $Li_{1.33}Mn_{0.67}O_2$ (PDF #04-014-7419) was used as reference. The calculated result is consistent with experimental data quite well. The calculated cell parameters from Rietveld refinement are listed in Figure 1c, in which the lattice parameters, a, b, c and volume, keep increasing with amount of Ti substitution, demonstrating that Ti^{4+} was successfully integrated into the lattice and substituted for Mn^{4+}. It is also consistent with the first-principles calculations (as shown in Table 1, the calculated volume increases from $Li_9(Mn_1Co_1Ni_1Mn_6)O_{18}$ to

$Li_9(Ti_1Co_1Ni_1Mn_6)O_{18}$, or from $Li_9(Mn_9)O_{18}$ to $Li_9(Ti_9)O_{18}$ for the cases without the effect of the effective Coulomb interaction U_{eff}).

Figure 2a –2c show SEM micrographs of the reference and Ti-substituted samples. It is seen that Ti substitution did not significantly change particle size or morphology. All three samples are agglomerates with crystallite sizes of 200 ~ 300 nm. Figure 2d – 2i show the cross-section TEM micrographs of the Ti-substituted sample with x=0.037 and the corresponding elements mapping. The particle size is ~300 nm, and Ti is uniformly distributed within the particle, indicating that the Ti^{4+} ions successfully diffuse into the transitional metal sublattice, instead of staying at particle surface.

XPS has been carried out to detect the valence state of the transitional metals in the Ti-free and -substituted samples and the results are summarized in Figure 3. It indicates that the 2p spectrum of each transitional metal split into two spin-orbit coupling components, namely, $2p_{3/2}$ and $2p_{1/2}$ in the Ti-free and -substituted samples. The $2p_{3/2}$ peaks of Mn, Co and Ni in those samples occurred at binding energies of approximately 642, 780 and 855 eV, respectively, which are fairly analogous to that for Mn^{4+}, Co^{3+} and Ni^{2+}.[45] The $2p_{3/2}$ peak of Ti in the Ti-substituted samples occurred at binding energy of ~ 458 eV, coming close to the values of Ti^{4+}.[46] XPS results further confirmed that Ti^{4+} successfully substituted for Mn^{4+} in the composite as expected and substitution of Ti^{4+} for Mn^{4+} does not change the valences of Ni and Co.

Figure 4a shows the first charge/discharge voltage profiles of the reference and Ti-substituted samples between 2 and 4.8 V at C/10 rate (1C = 248 $mAhg^{-1}$). The charging profiles of all

samples have distinct slope and plateau regions. The slope region, before charging to 4.4 V, corresponds to the oxidization of Ni from valence 2+ to 4+ and Co from 3+ to 4+.[47] All these three samples show similar specific capacity in the slope region, suggesting that the substitution of Ti^{4+} for Mn^{4+} does not change the valences of Ni and Co, which coincides with the XPS results. The plateau higher than 4.4 V corresponds to the oxidation of O^{2-} and the loss of lithium and oxygen from the Li_2MnO_3 component. According to Kim *et al.*,[37] this process can be represented by the following reactions.

$$Li_2MnO_3 \rightarrow 2Li^+ + Mn^{4+}O_3^{4-} + 2e^- \quad (1)$$

$$2Mn^{4+}O_3^{4-} \rightarrow 2MnO_2 + O_2 \quad (2)$$

During reaction (1), the configuration $Mn^{4+}O_3^{4-}$ forms by removing electrons from the oxygen 2p band, and further changes to MnO_2 in reaction (2). The net result of this two-step reaction leads to removing of Li^+ and O^{2-} ions with a 2:1 ratio (Li_2O) from the Li_2MnO_3 component. With increasing Ti content, the capacity in the plateau region decreases greatly, indicating Ti substitution restrains the oxidation of O^{2-} ions to O_2, which is consistent with previous reports.[24, 36] Figure 4b illustrates the cycling performance of these three samples under the same conditions. The pristine sample with $x = 0$ exhibits rapid capacity fading, dropping from 215.8 $mAhg^{-1}$ in the 1st cycle to 87.5 $mAhg^{-1}$ in the 150th cycle, a retention of only 37.5%. In comparison, the Ti-substituted samples with $x = 0.037$ and $x = 0.074$ deliver 159.8 and 146.1 $mAhg^{-1}$ after 150 cycles, corresponding to capacity retentions of 73.9 % and 81%, respectively.

As previously noted, voltage fading is a major issue of the Li- and Mn-rich layered cathode materials.[33] The voltage fading could be due to the following two reasons. First, acidic species in electrolyte attack the electrode that causes the deterioration of the electrode/electrolyte interface.

Second and more importantly, the intrinsic structure transforms from layered to spinel-like due to Mn ions migration.[10] The structure transformation leads to the evolution of a redox reaction at ca. 3.0 V.[11-13] Figure 5a – 5c show the voltage fading of the reference and Ti-substituted samples from the 10th cycle to the 130th cycle with normalized discharge capacity. It is evident from Figure 5a that the voltage fading of the pristine sample with $x = 0$ is quite severe. The voltage at 50% depth of discharge (DOD) drops from 3.387 V in the 2nd cycle to 2.64 V in the 130th cycle. The Ti-substituted samples with $x = 0.037$ and $x = 0.074$ are shown in Figure 5b and Figure 5c, respectively. Their voltages at 50% DOD are 3.393 and 3.337 V in the 2nd cycle, and 2.852 and 2.915 V for the 130th cycle, respectively. Detailed comparison in discharge capacity above and below 3.5 V is shown in Figure 5d and 5e, to further investigate the effect of Ti on suppressing voltage fading. Figure 5d clearly illustrates that Ti-substituted samples exhibit significantly reduced capacity decay above 3.5 V, indicating a suppression of layered to spinel-like structure transformation. Unfortunately, the structure transformation could not be totally avoided by Ti substitution, as reflected by the decreased capacity above 3.5 V and the concurrently increased capacity below 3.5 V (Figure 5e).

DFT calculations were carried out to further understand the effects of Ti substitution on improving the cycling stability and suppressing the voltage fading. Calculated properties are summarized in Table 1 for the layered cathode materials $Li_9(X_1Y_1Z_1Mn_6)O_{18}$ (X, Y, and Z = Co, Li, Mn, Ni, and Ti) and their endmembers $Li_9(M_9)O_{18}$ (M =Co, Li, Mn, Ni, and Ti) with and without the effect of the effective Coulomb interaction U_{eff}. The fitted results using a four-parameter Birch-Murnaghan equation of state (EOS)[48] (see detailed methodology in SI) include equilibrium volume (V_0), bulk modulus (B_0) and its first derivative with respect to pressure (B_0'),

enthalpy of mixing (H_{mix}) with respect to the reference states of endmembers, cohesive energy (E_{coh}) with respect to the reference states of free atoms, and magnetic moment per metal atom within the metal-sublattice. It is worth mentioning that the predicted magnetic moments for the free atoms are 1, 2, 2, 3, 3.5, and 5 μ_B/atom for Li, O, Ni, Co, Ti, and Mn, respectively. Without the effect of U_{eff}, the predicted V_0, B_0, and B_0' of $LiCoO_2$ agree well with previous experiments,[49, 50] while predictions from PBEsol+U_{eff} give a larger V_0 (8% larger) and a smaller B_0 (22% smaller) due to the effect of U_{eff}, see Table 1. However, the magnetic nature[51] of $LiCoO_2$ can only be predicted using PBEsol+U_{eff}, and the present work predicts a similar magnetic moment (2 μ_B/Co-atom) as other predictions using the GGA+U method.[52] In particular, without U_{eff}, large fluctuation of magnetic moment as a function of volume exists for elements Co, Mn, and Ni, leading to scattered volume-energy data points (see details in Table 1). Hence, both PBEsol and PBEsol+U_{eff} are employed in the present work with latter one being the main choice.

For a better understating of first-principles results, Figure 6 illustrates the cohesive energies of $Li_9(X_1Y_1Z_1Mn_6)O_{18}$ and $Li_9(M_9)O_{18}$ as listed in Table 1. It can be seen that the strongest and weakest bonding are for $Li_9(Ti_9)O_{18}$ and $Li_9(Li_9)O_{18}$, respectively. These cohesive energies indicate that the more content of alloying element Ti, the lower the cohesive energy of the layered cathode materials studied herein (i.e., the more stable they are). For example, the cohesive energy of $Li_9(Ti_2Co_1Mn_6)O_{18}$ is lower than that of $Li_9(Ti_1Co_2Mn_6)O_{18}$. Table 1 also shows that the enthalpies of mixing H_{mix} for $Li_9(X_1Y_1Z_1Mn_6)O_{18}$ are all negative, especially for the cases predicted from PBEsol+U_{eff}. These negative values of H_{mix} indicate that the mixing of different alloying elements (X, Y, and Z) will make the $Li_9(X_1Y_1Z_1Mn_6)O_{18}$ more stable. It should be noted that the H_{mix} values listed in Table 1 cannot be used to judge the phase stability due to different chemistry of $Li_9(X_1Y_1Z_1Mn_6)O_{18}$. In addition, it is shown in Table 1 that the

values of cohesive energy are consistent with phonon calculations: the layered cathode materials with higher cohesive energies (e.g.,> -5.1 eV/atom) are structurally unstable, as indicated by the appearance of imaginary phonon modes ($Li_9(Li_1Co_1Ni_1Mn_6)O_{18}$is one example of this). Note that the verification of phonon calculations is given in the SI, including the phonon density of state of $LiCoO_2$ (see Figure S4) and the Raman and infrared phonon frequencies at the Γ point of $LiCoO_2$ (see Table S1), which agree reasonably well with experimental data. As shown in Figure S3, it is further found that the larger the bulk modulus, the lower the cohesive energy for these cathode materials, implying that bulk modulus can be used as an indicator to judge the structural stability of these layered cathode materials.

In an effort to analyze the interactions between each atomic pair quantitatively, Figure 7 illustrates an example of the key stretching force constants of $Li_9(Ti_1Co_1Ni_1Mn_6)O_{18}$ predicted by PBEsol+U_{eff} at its theoretical equilibrium volume at 0 K (see Table 1). It is a known fact that force constants quantify the extent of interaction between atoms.[43, 53, 54] A large positive force constant suggests strong interaction, while a negative force constant suggests that the two atoms in question would prefer to move apart. A zero or near-zero force constant indicates that the interactions between two atoms are negligible. Figure 6 shows that the O-Ti and O-Mn atomic pairs possess similar-strength interactions, the strongest among all the atomic pairs. These are key atomic pairs to stabilize the octahedral cage formed by oxygen and metals (see Figure S5 in SI), and in turn, the whole structure of $Li_9(X_1Y_1Z_1Mn_6)O_{18}$. Concerning the metal-metal pairs within the metal-sublattice, the strongest interaction is for the Mn-Ti pair (see Figure 6), further indicating the role of Ti in preventing the Mn ion migration. Additionally, the range of charge loss for Ti is the largest one among all metals (see Figure S6), implying again that the addition of Ti will stabilize the layered structure.

Combining all of these results, first-principles and phonon calculations indicate that the substitution of Ti into the Li- and Mn-rich cathode material can reduce the whole cohesive energy, stabilizing the layered structure. Also, strong interaction between Ti and Mn will prevent the migration of Mn to the adjacent Li ion layer, restrain formation of the spinel structure, and consequently weaken the voltage fading.[27, 55]

Figure 8a compares the rate capability of the reference and Ti-substituted samples. In Figure 8a, with increased charge/discharge rates from 0.1C to 5C, the pristine sample (x = 0) delivers the specific discharge capacity from ~240 to 100 $mAhg^{-1}$. In comparison, specific discharge capacity decreases from ~220 to 105 $mAhg^{-1}$ for the sample with x = 0.037, and from ~170 to 30 $mAhg^{-1}$ for the sample with x = 0.074. The Ti-substituted sample with x = 0.074 exhibits the poorest rate capability, which is mainly due to the substitution of insulating Ti^{4+} ions. Figure 8b compares the normalized discharge capacities of the Ti-substituted cathode samples at different rates. It shows that the sample with x = 0.037 possesses the best rate capability. This can be explained by the following reasons. During cycling, structure transformation from layer to spinel, caused by Mn migration into the Li ion site (Li-sublattice), induces large structure distortion, which blocks the Li migration path,[32] deteriorating the rate capability.[31, 56] Therefore, the rate capability of the pristine sample is not good, especially at high current density (4C and 5C). As indicated by the present first-principles and phonon calculations, Ti-Mn pair has stronger interaction than the Mn-Mn pair, meaning that Ti substitution can stabilize Mn, and thus, restraining Mn migration into Li ion layer. Therefore, the $Li[Li_{0.26}Mn_{0.563}Ti_{0.037}Ni_{0.07}Co_{0.07}]O_2$ electrode with moderate conductivity and alleviated Mn migration shows the best rate performance. While further

increase of Ti content, the electronic conductivity of the $Li[Li_{0.26}Mn_{0.526}Ti_{0.074}Ni_{0.07}Co_{0.07}]O_2$ decreases due to the electronically insulating nature of Ti^{4+} cations, leading to even poorer rate performance.

■ SUMMARY

In an effort to synthesize high-energy-density, Li- and Mn-rich layered cathode materials with improved structural stability and suppressed voltage fading, an integrated approach of simulation and experiment has been employed in the present work for the layered Li- and Mn-rich cathode materials $Li[Li_{0.26}Mn_{0.6-x}Ti_xNi_{0.07}Co_{0.07}]O_2$ ($0<x<0.1$). First-principles and phonon calculations indicates that (i) cohesive energy can be used to judge the phase stability of $LiMO_2$, and Ti is found to be the most favorite alloying element among Mn, Co, and Ni; (ii) Ti can help to stabilize Mn, prevent Mn migration to Li ion layer, and therefore, suppress the voltage fading. As a case study, structural and electrochemical properties of the layered cathode materials $Li[Li_{0.26}Mn_{0.6-x}Ti_xNi_{0.07}Co_{0.07}]O_2$ have been characterized and analyzed by XRD, TEM and galvanostatic charge/discharge process. It is found that alloying element Ti indeed extends the cathode's cycling life and weakens the voltage fading. A high initial specific capacity of ~220 $mAhg^{-1}$ and a cycling retention of 73.9%, and good rate capabilityare achieved after optimized Ti substitution in the $Li[Li_{0.26}Mn_{0.563}Ti_{0.037}Ni_{0.07}Co_{0.07}]O_2$ material.

■ ASSOCIATED CONTENT

Supporting Information

Detail of first-principles and phonon calculations together with their results. This material is accessible online and free of charge at http://pubs.acs.org.

■AUTHOR INFORMATION

Corresponding Author

*E-mail:dr.liu@psu.edu

*E-mail:dwang@psu.edu

Notes

The authors declare no competing financial interest.

■ACKNOWLEDGMENTS

This work was financially supported by NSF with Grant No. DMR-1310289. First-principles calculations were carried out partially on the LION clusters at the Pennsylvania State University, partially on the resources of NERSC supported by the Office of Science of the U.S. Department of Energy under contract No. DE-AC02-05CH11231, and partially on the resources of XSEDE supported by NSF with Grant No. ACI-1053575.

■REFERENCES

1. J. M. Tarascon and M. Armand, *Nature*, 2001, 414, 359-367.
2. M. S. Whittingham, *Chem. Rev.*, 2004, 104, 4271-4301.
3. S. L. Brock, N. Duan, Z. R. Tian, O. Giraldo, H. Zhou and S. L. Suib, *Chem. Mater.*, 1998, 10, 2619-2628.
4. G. Rousse and J. M. Tarascon, *Chem. Mater.*, 2014, 26, 394-406.
5. A. Manthiram and J. Kim, *Chem. Mater.*, 1998, 10, 2895-2909.
6. V. Etacheri, R. Marom, R. Elazari, G. Salitra and D. Aurbach, *Energy Environ. Sci.*, 2011, 4, 3243-3262.
7. H. Li, Z. Wang, L. Chen and X. Huang, *Adv. Mater.*, 2009, 21, 4593-4607.
8. Z. Yu, J. Song, M. L. Gordin, R. Yi, D. Tang and D. Wang, *Advanced Science*, 2015, 2: . doi: 10.1002/advs.201400020.
9. J. W. Fergus, *J. Power Sources*, 2010, 195, 939-954.
10. Y. Wang and G. Cao, *Adv. Mater.*, 2008, 20, 2251-2269.
11. A. Kraytsberg and Y. Ein-Eli, *Adv. Energy Mater.*, 2012, 2, 922-939.
12. B. Ammundsen and J. Paulsen, *Adv. Mater.*, 2001, 13, 943-956.
13. R. Marom, S. F. Amalraj, N. Leifer, D. Jacob and D. Aurbach, *J. Mater. Chem.*, 2011, 21, 9938-9954.
14. B. L. Ellis, K. T. Lee and L. F. Nazar, *Chem. Mater.*, 2010, 22, 691-714.
15. B. Xu, D. Qian, Z. Wang and Y. S. Meng, *Mater. Sci. Eng. R.*, 2012, 73, 51-65.
16. B. Qiu, J. Wang, Y. Xia, Z. Wei, S. Han and Z. Liu, *ACS Appl. Mater. Interfaces*, 2014, 6, 9185-9193.
17. P. He, H. Yu, D. Li and H. Zhou, *J. Mater. Chem.*, 2012, 22, 3680-3695.
18. X. Yang, X. Wang, L. Hu, G. Zou, S. Su, Y. Bai, H. Shu, Q. Wei, B. Hu, L. Ge, D. Wang and L. Liu, *J. Power Sources*, 2013, 242, 589-596.
19. K. Du, F. Yang, G.-r. Hu, Z.-d. Peng, Y.-b. Cao and K. S. Ryu, *J. Power Sources*, 2013, 244, 29-34.
20. M. Hu, X. Pang and Z. Zhou, *J. Power Sources*, 2013, 237, 229-242.
21. Z. Lu, D. D. MacNeil and J. R. Dahn, *Electrochem. Solid St*, 2001, 4, A191-A194.
22. Y.-K. Sun, M.-J. Lee, C. S. Yoon, J. Hassoun, K. Amine and B. Scrosati, *Adv. Mater.*, 2012, 24, 1192-1196.
23. B. Song, Z. Liu, M. O. Lai and L. Lu, *Phys. Chem. Chem. Phys.*, 2012, 14, 12875-12883.
24. Z. Q. Deng and A. Manthiram, *J. Phys. Chem. C*, 2011, 115, 7097-7103.
25. M. M. Thackeray, S.-H. Kang, C. S. Johnson, J. T. Vaughey, R. Benedek and S. A. Hackney, *J. Mater. Chem.*, 2007, 17, 3112-3125.
26. C. S. Johnson, N. Li, C. Lefief and M. M. Thackeray, *Electrochem. Commun.*, 2007, 9, 787-795.
27. G. He, Y. Li, J. Li and Y. Yang, *Electrochem. Solid St*, 2010, 13, A19.
28. B. Song, H. Liu, Z. Liu, P. Xiao, M. O. Lai and L. Lu, *Sci. Rep.*, 2013, 3, 3094-3094.
29. S. Wang, J. Yang, X. Wu, Y. Li, Z. Gong, W. Wen, M. Lin, J. Yang and Y. Yang, *J. Power Sources*, 2014, 245, 570-578.
30. M. M. Thackeray, C. S. Johnson, J. T. Vaughey, H. N. LiCurrent address: eVionyx Inc and S. a. Hackney, *J. Mater. Chem.*, 2005, 15, 2257-2257.
31. J. Reed, G. Ceder and A. Van Der Ven, *Electrochem. Solid St*, 2001, 4, A78.
32. J. Zheng, M. Gu, J. Xiao, P. Zuo, C. Wang and J.-G. G. Zhang, *Nano Lett.*, 2013, 13, 3824-3830.
33. J. R. Croy, D. Kim, M. Balasubramanian, K. Gallagher, S.-H. Kang and M. M. Thackeray, *J. Electrochem. Soc.*, 2012, 159, A781.
34. B. Xu, C. R. Fell, M. Chi and Y. S. Meng, *Energy Environ. Sci.*, 2011, 4, 2223-2233.
35. X. Dong, Y. Xu, L. Xiong, X. Sun and Z. Zhang, *J. Power Sources*, 2013, 243, 78-87.
36. C.-C. Wang and A. Manthiram, *J. Mater. Chem. A*, 2013, 1, 10209-10209.

37. J.-S. Kim, C. S. Johnson, J. T. Vaughey, M. M. Thackeray, S. A. Hackney, W. Yoon and C. P. Grey, *Chem. Mater.*, 2004, 16, 1996-2006.
38. Z. Li, N. A. Chernova, J. Feng, S. Upreti, F. Omenya and M. S. Whittingham, *J. Electrochem. Soc.*, 2011, 159, A116-A120.
39. K. Jeom-Soo, S. J. Christopher, T. V. John, M. T. Michael, A. H. Stephen, Y. Wonsub and P. G. Clare, *Chem. Mater.*, 2004, 16.
40. G. Kresse and J. Furthmüller, *Phys. Rev. B*, 1996, 54, 11169-11186.
41. J. P. Perdew, A. Ruzsinszky, G. I. Csonka, O. A. Vydrov, G. E. Scuseria, L. A. Constantin, X. Zhou and K. Burke, *Phys. Rev. Lett.*, 2008, 100, 136406.
42. S. Shang, Y. Wang, W. Y. Wang, H. Fang and Z.-K. Liu, *Appl. Phys. Lett.*, 2013, 103, 053903.
43. S. L. Shang, Y. Wang, Z. G. Mei, X. D. Hui and Z. K. Liu, *J. Mater. Chem.*, 2012, 22, 1142-1149.
44. Y. Wang, S. Shang, Z.-K. Liu and L.-Q. Chen, *Phys. Rev. B*, 2012, 85, 224303.
45. J.-H. Park, J. Lim, J. Yoon, K.-S. Park, J. Gim, J. Song, H. Park, D. Im, M. Park, D. Ahn, Y. Paik and J. Kim, *Dalton Transactions*, 2012, 41, 3053-3059.
46. R. Castillo, B. Koch, P. Ruiz and B. Delmon, *J. Catal.*, 1996, 161, 524-529.
47. C. S. Johnson, J. S. Kim, C. Lefief, N. Li, J. T. Vaughey and M. M. Thackeray, *Electrochem. Commun.*, 2004, 6, 1085-1091.
48. S.-L. Shang, Y. Wang, D. Kim and Z.-K. Liu, *Comp. Mater. Sci.*, 2010, 47, 1040-1048.
49. Y. Takahashi, N. Kijima, K. Dokko, M. Nishizawa, I. Uchida and J. Akimoto, *J. Solid State Chem.*, 2007, 180, 313-321.
50. X. Wang, I. Loa, K. Kunc, K. Syassen and M. Amboage, *Phys. Rev. B*, 2005, 72, 224102.
51. J. T. Hertz, Q. Huang, T. McQueen, T. Klimczuk, J. W. G. Bos, L. Viciu and R. J. Cava, *Phys. Rev. B*, 2008, 77, 075119.
52. F. Xiong, H. J. Yan, Y. Chen, B. Xu, J. X. Le and C. Y. Ouyang, *International Journal of Electrochemical Science*, 2012, 7, 9390-9400.
53. S. L. Shang, L. G. Hector, Y. Wang, H. Zhang and Z. K. Liu, *Journal of Physics-Condensed Matter*, 2009, 21, 246001.
54. S.-L. Shang, L. G. Hector Jr, S. Shi, Y. Qi, Y. Wang and Z.-K. Liu, *Acta Mater.*, 2012, 60, 5204-5216.
55. M. M. Thackeray, C. S. Johnson, J. S. Kim, K. C. Lauzze, J. T. Vaughey, N. Dietz, D. Abraham, S. A. Hackney, W. Zeltner and M. A. Anderson, *Electrochem. Commun.*, 2003, 5.
56. A. Ito, K. Shoda, Y. Sato, M. Hatano, H. Horie and Y. Ohsawa, *J. Power Sources*, 2011, 196, 4785-4790.

Table 1. Calculated properties of the layered cathode materials $Li_9(X_1Y_1Z_1Mn_6)O_{18}$ and their endmembers $Li_9(M_9)O_{18}$ with and without the effect of U_{eff}, including structural stability identified by phonon modes, equilibrium volume (V_0, Å^3/atom), bulk modulus (B_0, GPa), the first derivative of bulk modulus with respect to pressure (B_0'), enthalpy of mixing (H_{mix}, meV/atom) with respect to the endmembers (i.e., the first five materials below), cohesive energy (E_{coh}, ev/atom) with respect to free atoms, and magnetic moment per metal in the metal sublattice (MM, μ_B).

Materials	Abbr.	Note	Phonon	V_0	B_0	B_0'	H_{mix}	E_{coh}	MM
$Li_9(Co_9)O_{18}$	Co_9	With U_{eff}	Stable	8.708	115.7	4.35	0	-5.51	2
		Without U_{eff}	Stable	7.980	152.9	4.42	0	-5.28	0
		Expt.		8.04[a]	149±2[b]	4.1±0.3[b]			5.9[c]
$Li_9(Li_9)O_{18}$	Li_9	Without U_{eff}	Unstable	7.786	75.1	4.14	0	-3.58	
$Li_9(Mn_9)O_{18}$	Mn_9	With U_{eff}	Unstable	9.283	111.2	4.38	0	-4.76	4
		Without U_{eff}	Stable	8.162	152.8	4.47	0	-5.21	2
$Li_9(Ni_9)O_{18}$	Ni_9	With U_{eff}	Unstable	8.318	125.5	4.31	0	-5.10	1
		Without U_{eff}	Stable[d]	8.333	134.1	4.37	0	-4.87	1
$Li_9(Ti_9)O_{18}$	Ti_9	Without U_{eff}	Stable	8.930	138.5	4.45	0	-6.40	
$Li_9(Mn_1Co_1Ni_1Mn_6)O_{18}$	$Mn_1Co_1Ni_1$	With U_{eff}	Stable	9.005	115.3	4.55	-122.1	-5.00	31/9
		Without U_{eff}		8.258	141.7	4.63	-15.5	-5.19	17/9
$Li_9(Co_1Co_1Ni_1Mn_6)O_{18}$	Co_2Ni_1	With U_{eff}	Stable[d]	8.883	120.7	4.43	-138.7	-5.10	29/9
		Without U_{eff}		8.377	128.2	4.22	-12.0	-5.20	23/9[e]
$Li_9(Ti_1Co_1Ni_1Mn_6)O_{18}$	$Ti_1Co_1Ni_1$	With U_{eff}	Stable[d]	8.922	118.8	4.43	-128.2	-5.19	28/9
		Without U_{eff}		8.375	141.0	4.48	-30.3	-5.34	18/9[e]
$Li_9(Ti_1Co_1Co_1Mn_6)O_{18}$	Ti_1Co_2	With U_{eff}	Stable	9.137	116.3	4.35	-130.2	-5.24	29/9
		Without U_{eff}		8.348	170.3	5.86	-16.9	-5.37	19/9[e]
$Li_9(Ti_1Co_1Ti_1Mn_6)O_{18}$	Ti_2Co_1	With U_{eff}	Stable	9.201	111.6	4.70	-125.2	-5.33	28/9
		Without U_{eff}		8.730	173.1	4.00	-3.1	-5.48	22.2/9[e]
$Li_9(Li_1Co_1Ni_1Mn_6)O_{18}$	$Li_1Co_1Ni_1$	With U_{eff}	Unstable	8.703	114.8	4.48	-222.9	-4.97	25/9
		Without U_{eff}		8.335	132.8	4.54	-178.1	-5.18	21/9

[a]Measurements at room temperature.[49]
[b]Measurements by fitting the pressure-volume data points.[50]
[c]Measurements of high spin magnetic moment,[51] while other predictions using the GGA+U method give $2\mu_B$ per Co-atom.[52]
[d]A few imaginary phonon modes exist (less than < 0.5%) may due to the settings of first-principles calculations.
[e]These results are for reference only due to the fluctuation of magnetism as a function of volume.

Figures and Figure Captions

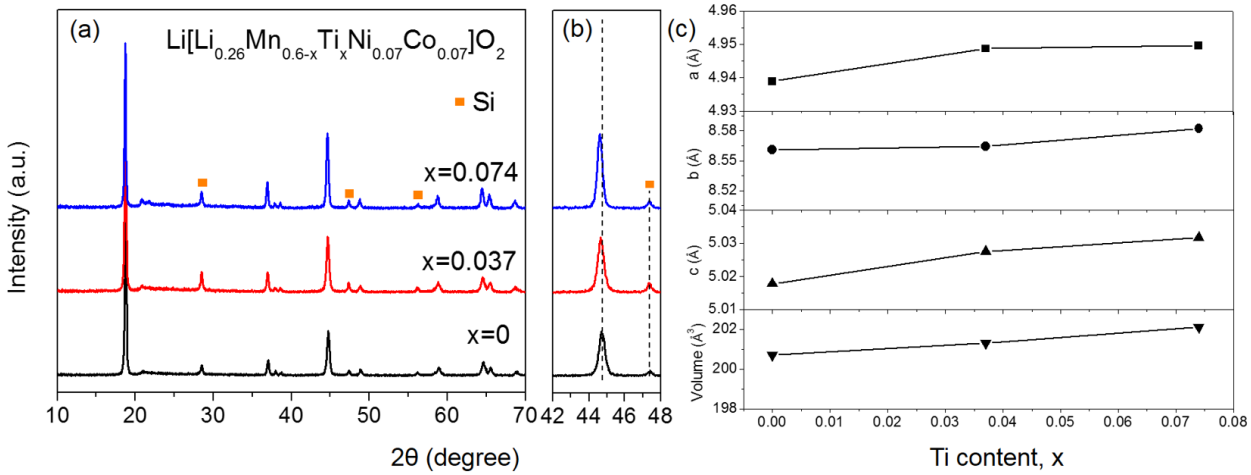

Figure 1 (a) X-ray diffraction patterns of $Li[Li_{0.26}Mn_{0.6-x}Ti_xNi_{0.07}Co_{0.07}]O_2$ samples (x = 0, 0.037 and 0.074) with Si as internal standard marked as yellow square; (b) magnified 2θ region of 43-46°; and (c) the calculated lattice parameters.

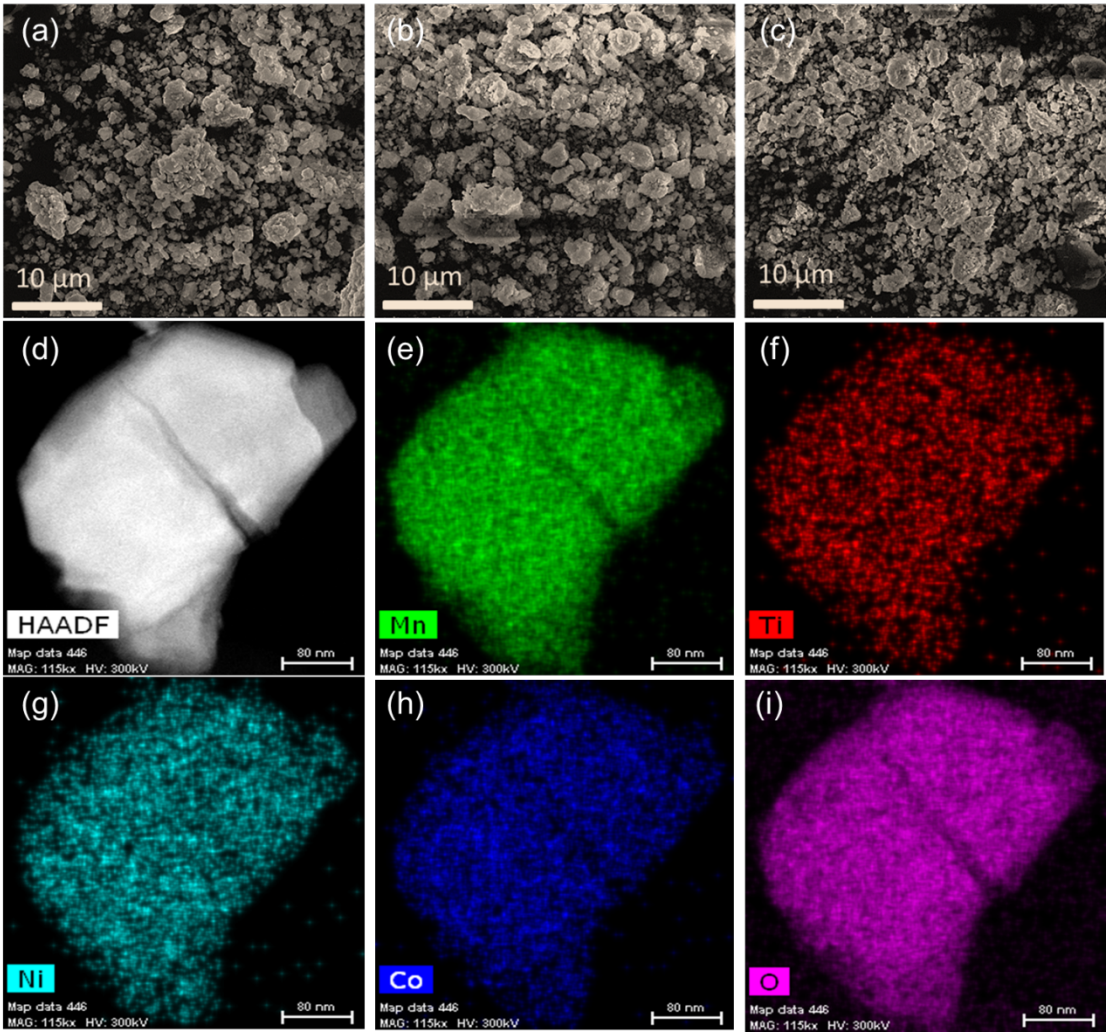

Figure 2 SEM micrographs of $Li[Li_{0.26}Mn_{0.6-x}Ti_xNi_{0.07}Co_{0.07}]O_2$ samples: (a) $x = 0$; (b) $x = 0.037$; (c) $x = 0.074$; (d) Cross-section STEM image of Ti-substituted sample $Li[Li_{0.26}Mn_{0.563}Ti_{0.037}Ni_{0.07}Co_{0.07}]O_2$; and the corresponding element mapping of (e) Mn; (f) Ti; (g) Ni; (h) Co; and (i) O.

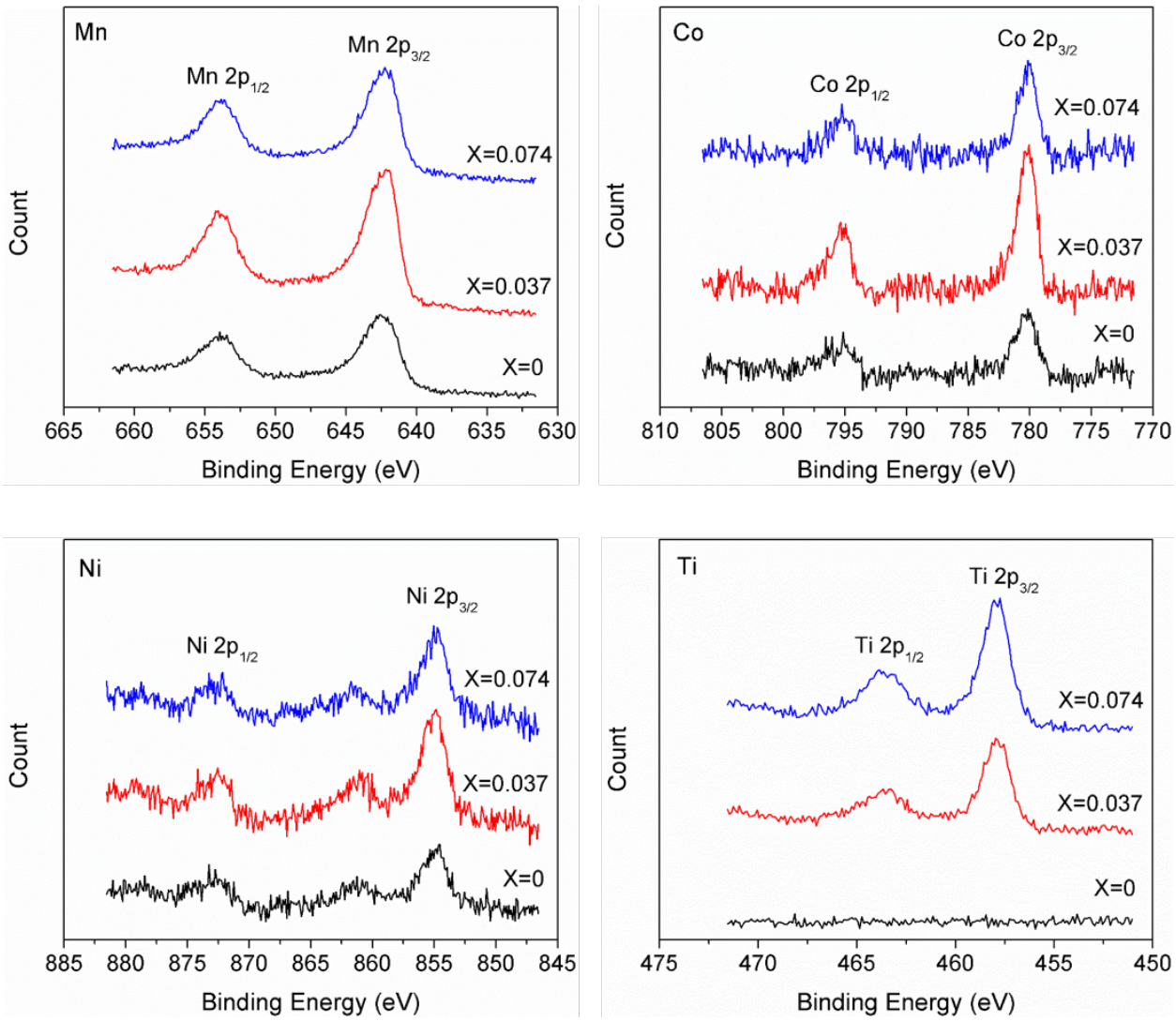

Figure 3 XPS results for transitional metals of Mn, Co, Ni and Ti in the samples $Li[Li_{0.26}Mn_{0.6-x}Ti_xNi_{0.07}Co_{0.07}]O_2$ with $x = 0$, 0.037 and 0.074.

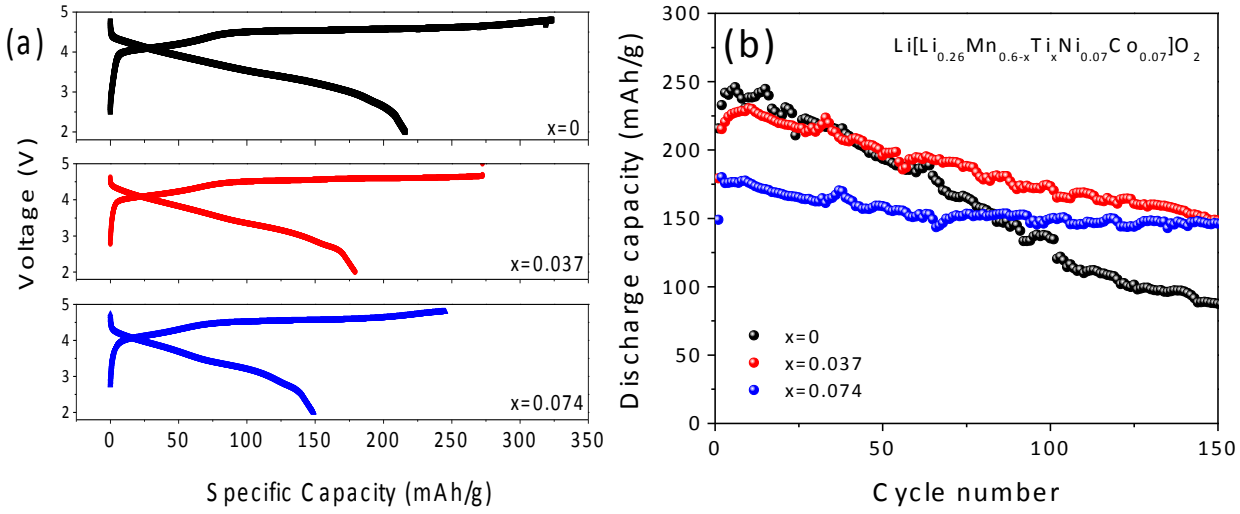

Figure 4 (a) First cycle voltage profiles of the Ti-substituted cathode samples $Li[Li_{0.26}Mn_{0.6-x}Ti_xNi_{0.07}Co_{0.07}]O_2$ (x = 0, 0.037, and 0.74); and (b) cycling performance of the Ti-substituted cathode samples $Li[Li_{0.26}Mn_{0.6-x}Ti_xNi_{0.07}Co_{0.07}]O_2$ (x = 0, 0.037, and 0.074).

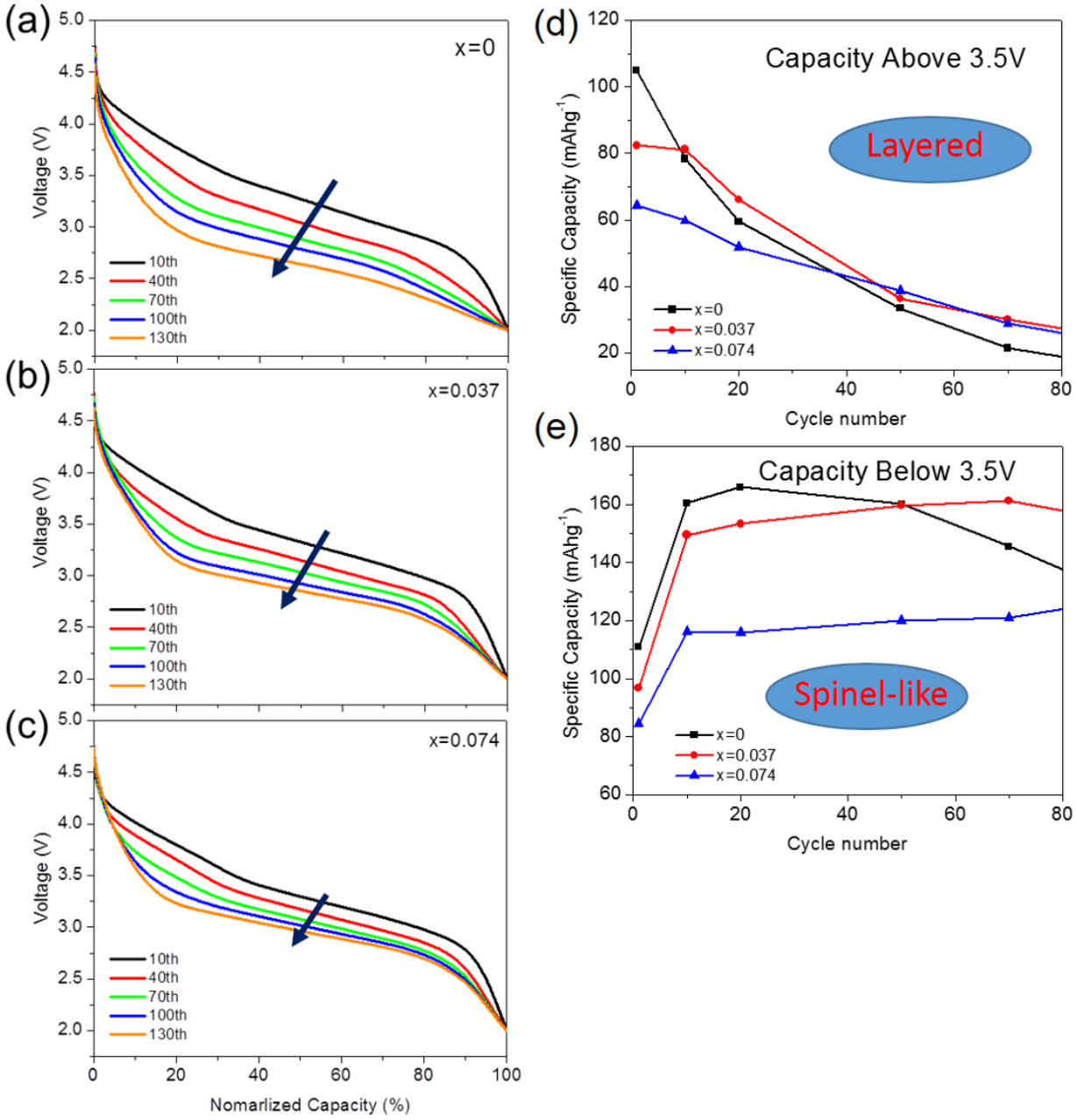

Figure 5 Voltage fading of the $Li[Li_{0.26}Mn_{0.6-x}Ti_xNi_{0.07}Co_{0.07}]O_2$ samples: (a) $x = 0$; (b) $x = 0.036$; and (c) $x = 0.074$, with normalized discharge capacity; (d) discharge capacity above 3.5 V during cycling of the three samples; (e) discharge capacity below 3.5 V during cycling of the three samples.

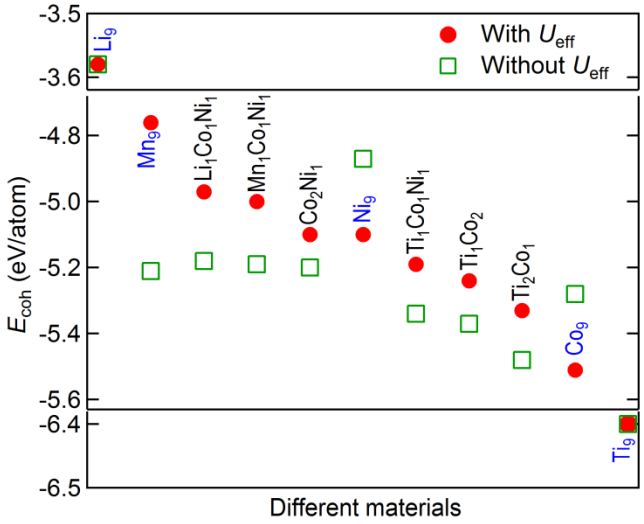

Figure 6 Cohesive energies of $Li_9(X_1Y_1Z_1Mn_6)O_{18}$ and their endmembers $Li_9(M_9)O_{18}$ (X, Y, Z and M = Li, Co, Mn, Ni, and Ti) predicted by exchange-correction of PBEsol with and without the effect of U_{eff}. Note that $X_1Y_1Z_1$ and M_9 within in the metal-sublattice are used to label each material, and their full names are given shown in Table 1.

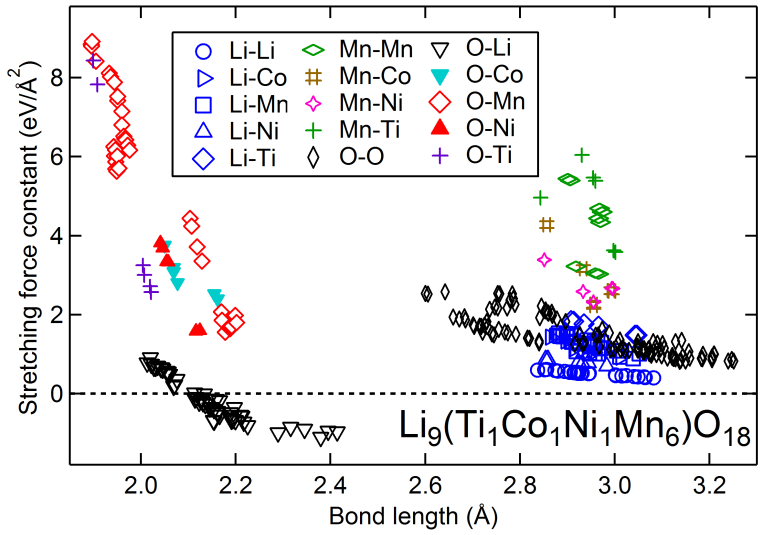

Figure 7 Key stretching force constants of $Li_9(Ti_1Co_1Ni_1Mn_6)O_{18}$ from first-principles phonon calculations for each atomic pair predicted by PBEsol+U_{eff}. Note that a large positive force constant suggests strong interaction.

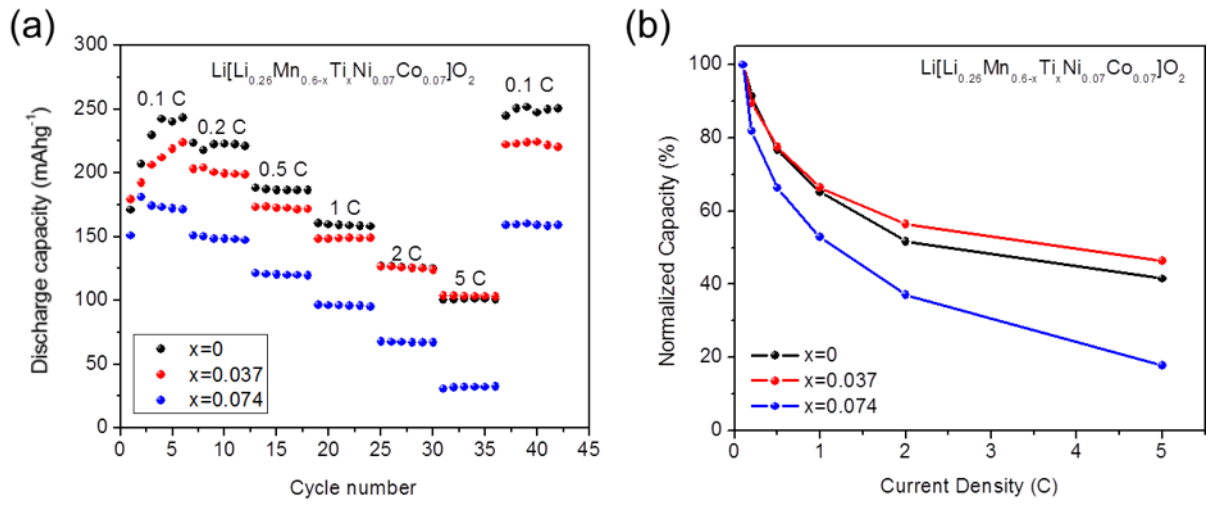

Figure 8 (a) Rate performance of the $Li[Li_{0.26}Mn_{0.6-x}Ti_xNi_{0.07}Co_{0.07}]O_2$ (x = 0, 0.037, and 0.074) samples; and (b) the normalized discharge capacity at different C rates (1C = 242 $mAhg^{-1}$).

Ti-substituted $Li[Li_{0.26}Mn_{0.6-x}Ti_xNi_{0.07}Co_{0.07}]O_2$ cathode shows extended cycle life and mitigated voltage fading due to Ti substitution and its improved stability of the Li- and Mn-rich layered structure.